

Article

Trajectories of Graphitizable Anthracene Coke and Non-Graphitizable Sucrose Char during the Earliest Stages of Annealing by Rapid CO₂ Laser Heating

Joseph P. Abrahamson ¹ , Abhishek Jain ², Adri C. T. van Duin ² and Randy L. Vander Wal ^{1,2,*}

¹ The EMS Energy Institute & Department of Energy and Mineral Engineering, The Pennsylvania State University, University Park, PA 16802, USA; joeabe162@gmail.com

² Department of Mechanical and Nuclear Engineering, The Pennsylvania State University, University Park, PA 16802, USA; azj126@psu.edu (A.J.); acv13@enr.psu.edu (A.C.T.v.D.)

* Correspondence: ruv12@psu.edu; Tel.: +1-814-865-5813

Received: 12 May 2018; Accepted: 7 June 2018; Published: 11 June 2018



Abstract: The earliest stages of annealing of graphitizable anthracene coke and non-graphitizable sucrose char were observed by rapid heating with a CO₂ laser. Structural transformations were observed with transmission electron microscopy. Anthracene coke and sucrose char were laser heated to 1200 °C and 2600 °C for 0.25–300 s. The transformations are compared to traditional furnace heating at matching temperatures for a 1 h duration. Traditional furnace and CO₂ laser annealing followed the same pathway, based upon equivalent end structures. Graphitizable anthracene coke annealed faster than non-graphitizable sucrose char. Sucrose char passed through a structural state of completely closed shell nanoparticles that opened upon additional heat treatment and gave rise to the irregular pore structure found in the end product. The observed curvature in sucrose char annealed at 2600 °C results from shell opening. The initial presence of curvature and loss by heat treatment argues that odd membered rings are present initially and not formed upon heat treatment. Thus, odd membered rings are not manufactured during the annealing process due to impinging growth of stacks, but are likely present in the starting structure. The observed unraveling of the closed shell structure was simulated with ReaxFF.

Keywords: carbonization; laser annealing; mesophase; graphitization; carbon material; ReaxFF

1. Introduction

Kinetics and annealing trajectories during the earliest stages of carbon heat treatment are largely unknown [1]. The study of graphitization kinetics appears to have had its beginning in 1961, when two papers on the topic were presented at the Fifth Conference on Carbon at Penn State University. Fair and Collins [1] presented their study on d_{002} spacing decrease and change in electrical resistivity in a calcined petroleum coke heated between 2000 and 3000 °C for durations as short as 8 min and as long as 20 h. The samples were preheated to 800 °C by keeping them in the end of a resistance tube furnace and then rapidly inserting them into the hot center. Upon insertion, the furnace dropped 10 °C and recovered in 7 min. Furnace heating is limited to time scales no less than several minutes due to slow heating rates. On this time scale, the only material transformation that is rate-restricted is the layer plane spacing reduction. These rates with respect to temperature are now well-known for these time scales (several minutes, minimum) [1–6]. Since these early pioneering studies, the kinetics and annealing trajectories during the earliest stages of carbon heat treatment have received limited attention. Measuring kinetics of solid-state reactions at temperatures above 2000 °C are challenging experimentally. The experimental challenge is in the control of achieving short time durations at precise

elevated temperatures. A recent study utilized the fast heating rate of a miniature graphitization furnace found in an atomic absorption spectrometer [7]. The crystallite size in both the a-direction (L_a) and c-direction (L_c) achieved converged values within a minute at 3000 °C [7]. It was recently demonstrated that CO₂ laser annealing of carbon black is equivalent to furnace annealing based on equivalent end structures [8]. Therefore, CO₂ laser annealing can be used to study the kinetics and early transformation trajectories by rapid heating [8,9]. In this work, CO₂ laser heating is used to observe the rates and trajectories of a model graphitizable and non-graphitizable carbon during the earliest stages of annealing.

The seminal work of Franklin in 1951 generated much interest in the topic of graphitizability [10,11]. Since then, carbon heat treatment with an emphasis on structural transformation dependence with Heat-Treatment-Temperature (HTT) has received extensive study. A quantification of HTT was provided by Oberlin in 1984 [12]. Around the same time, Marsh and Crawford [13] verified Oberlin's work. The HTT diagram provided by Oberlin is divided into four stages. The annealing stages as defined are separated by temperature. The transitions between stages occur too fast to observe with traditional furnace annealing [12]. To this day, the kinetics of annealing are not well-known due to the slow heating and cooling rates of furnaces. Additionally, consensus has yet to be reached on the cause of non-graphitizability. Cross-linking of carbon lamellae is said to be the cause of non-graphitizability [4,11]. However, the structure of such cross-links is still under debate.

The short heating durations used here enable the annealing pathway of graphitizable and non-graphitizable carbons to be followed and contrasted. Monitoring the materials trajectory with respect to time at temperature provides insight into the nature and formation mechanism of cross-links found in heat-treated non-graphitizable carbon. The observed trajectory of non-graphitizable sucrose char is simulated with the Reactive Force Field Method (ReaxFF).

2. Materials and Methods

2.1. Material Selection

Anthracene (98+% purity was purchased from Alfa Aesar, Tewksbury, MA, USA) and sucrose (food grade sucrose of 99.9% purity obtained from Dunkin Donuts, State College, PA, USA) were selected as model graphitizing and non-graphitizing carbon precursors based on historical precedents [11,12,14,15].

2.2. Carbonization

Samples were prepared by carbonization in a tube bomb reactor. Ten grams of precursor were loaded into the 25 mL reactor body. The reactor was purged of oxygen with nitrogen. A preheated and aerated sand bath was used to bring the reactor to temperature. Heating duration and temperature were 5 h and 500 °C. Carbonization occurred under autogenous pressure (no pressure control), pressures reached ~6.9 MPa. Additional details and a schematic of the reactor have been provided elsewhere [15].

2.3. Heat-Treatment

2.3.1. Furnace

Furnace heat treatment was performed under an argon atmosphere in a Centorr Vacuum Industries series 45 graphitization furnace (Nashua, NH, USA). The furnace was heated at a rate of 25 °C a minute. Heat treatment temperatures of 1200 and 2600 °C were used to anneal samples for a duration of 1 h.

2.3.2. CO₂ Laser

A 250 Watt Synrad Firestar (Mukilteo, WA, USA) series F201 continuous wave CO₂ laser was used to heat anthracene coke and sucrose char. The laser was made to pulse by turning on and off

the radio frequency amplifier, controlled with a pulse generator. Samples were heated at 1200 and 2600 °C. The power of the laser beam was controlled via pulse width modulation. Rapid cycling the radio frequency signal (faster than the rise and fall times of the laser medium ~100 μ s) acts to reduce power and maintain a true continuous wave laser beam. The output beam diameter is 4 mm and primarily 10.6 μ m radiation. A Galilean beam expander was used to increase the beam diameter to 12 mm during 1200 °C annealing experiments. The beam expander assembly was easily moved in and out of the optical path depending on desired intensity (temperature). The optical path is shown in Figure 1.

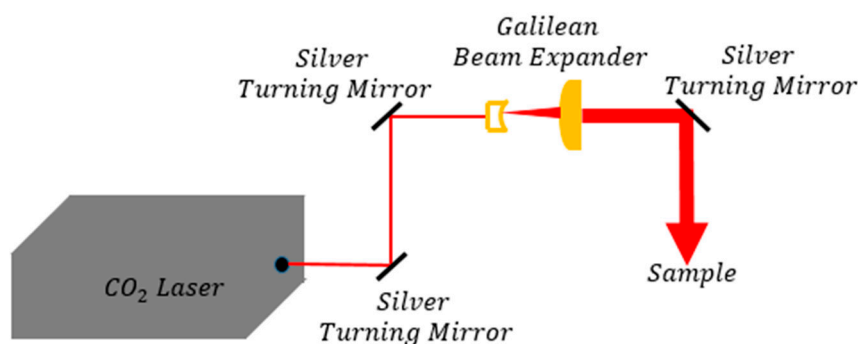


Figure 1. CO₂ laser beam path.

At 2600 °C, samples were heated as a thin powder layer, a few hundred microns thick, and held in a 3 mm wide and 2 mm deep hole in a graphite block. Samples were directly heated on transmission electron microscopy (TEM) grids when annealing with the beam expander in. Heating was performed under an argon atmosphere.

Multi-wavelength pyrometry was applied to determine the absolute temperature during laser annealing based on a black-body approximation. The carbons used in this study are well approximated as black-body absorbers, as evident by good fit of Planck's black-body radiation curves to the laser induced incandescence (LII) signal as displayed in Appendix A. Spectrally resolved Time-Temperature-Histories (TTHs) were recorded with a PI-Max[®] gated and intensified camera that was mounted on the 0.3 m spectrograph (Princeton Instruments, Trenton, NJ, USA). A multi-bundle fiber optic delivered LII signal to the camera system. The spectrograph-camera system was calibrated for both wavelength and detector response with respect to wavelength. A Hg-Ar lamp was used for wavelength calibration and a black-body tungsten lamp (HTS-94, Optronic Laboratories, Orlando, FL, USA) light source was used for detector calibration. The camera gate delay was synced to the laser trigger and stepped out to collect detailed TTHs.

2.4. Characterization

2.4.1. Diffraction

Lattice spacing (d_{002}) was measured by X-ray diffraction (XRD) from virgin and furnace annealed samples with a PANalytical Empyrean X-Ray Diffractometer (Westborough, MA, USA). Samples were analyzed in powder form and crushed with a mortar and pestle. To correct for instrument broadening, an external standard (silicon) was used. L_c and L_a were found by applying the Scherrer equation with dimensionless shape factor (K) values of 0.89 for L_c and 1.84 for L_a . Selected area electron diffraction (SAED) was used to measure the lattice spacing from laser-annealed materials where sample quantity was limited.

2.4.2. Transmission Electron Microscopy

TEM was used for direct visualization of nanostructure before and after annealing. Microscopy was performed on a FEI Talos operated at 200 keV (ThermoFisher Scientific, Hillsboro, OR, USA). Nanostructure (lamellae observed as (002) fringes) was observed in bright field mode at magnifications of 500,000. To aid in interpreting the 3-dimensional structure buried in the 2-dimensional projection, samples were tilted to both positive and negative angles.

2.4.3. Elemental Analysis

Energy Dispersive X-Ray Spectroscopy (EDS) was performed in the TEM in scanning mode for the purpose of measuring oxygen content. The resolution of EDS is limited to a few atomic % due to the background noise generated via Bremsstrahlung braking radiation.

2.4.4. Electron Energy Loss Spectroscopy

The conversion of sp^3 to sp^2 hybridized carbon was measured with Electron Energy Loss Spectroscopy (EELS) in a FEI Tecnai microscope (ThermoFisher Scientific, Hillsboro, OR, USA) fitted with a Gatan GIF Quantum[®] electron filter (Pleasanton, CA, USA). Measurements were calibrated against reference material that was furnace-annealed at 2600 °C for 1 h. The furnace annealed reference material is assumed to be 100% sp^2 (1:3 $\pi^*:\sigma^*$). The spectra background removal, plural scattering removal, peak fitting and integration were performed with the Gatan Digital Micrograph software (Pleasanton, CA, USA). The integrated area under the π^* edge was divided by the total area of the 20 eV wide carbon core loss envelope. Error is reported as the standard deviation about the mean from 3 measurements taken at different tilt angles, 0° and $\pm 40^\circ$.

2.5. ReaxFF Simulations

ReaxFF [16] is a bond-order based molecular dynamics (MD) framework [17]. ReaxFF uses the following expression to determine the forces on each atom:

$$E_{\text{system}} = E_{\text{bond}} + E_{\text{over}} + E_{\text{under}} + E_{\text{lp}} + E_{\text{val}} + E_{\text{tor}} + E_{\text{vdWaals}} + E_{\text{coulomb}}$$

where E_{bond} , E_{over} , E_{under} , E_{lp} , E_{val} , E_{tor} , E_{vdWaals} , and E_{coulomb} represent bond energy, over-coordination energy penalty, under-coordination stability, lone pair energy, valence angle energy, torsion angle energy, van der Waals energy, and coulomb energy, respectively. ReaxFF has been detailed elsewhere [16,18]. A range of carbon reactions have been successfully simulated with ReaxFF including pyrolysis and combustion of n-dodecane [19], coal [20], 1,6-dicyclopropane-2,4-hexyne [21] and JP-10 fuel [18].

Simulation Methodology

The initial structure constructed to mimic the experimental structure of sucrose char after 5 s at 2600 °C, consists of two fullerenic carbon spheres embedded within an outer shell. This is depicted in Figure 2. The structure consists of 2250 carbon atoms. The MD simulations are performed by keeping the number of atoms in a constant volume. The temperature is kept constant by using the Berendsen thermostat [22]. This configuration is designated as NVT. The system created is first minimized at a 727 °C for 100 ps. It is then ramped up to 3327 °C and equilibrated at this temperature. The MD time step used is 0.1 fs. The time step for an MD simulation should be one order of magnitude smaller than the highest frequency of molecules (approximately 0.5–1 fs). A time step of 0.1 fs ensures efficient coverage of the phase space and allows the reaction to occur smoothly. The force field used here is an extension [23] of the original CHO force field [18].

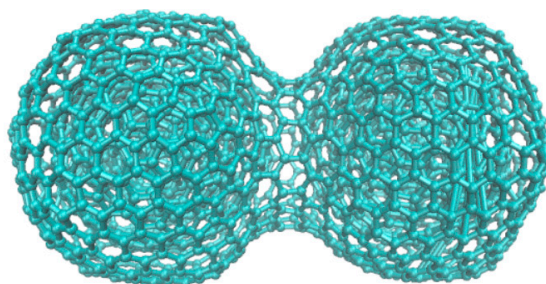


Figure 2. Carbon shell structure composed to mimic sucrose char behavior.

3. Results and Discussion

3.1. Carbonization and Furnace Annealing

The materials were furnace annealed to provide a reference for laser annealed material. The carbonized products of anthracene and sucrose result in a coke and a char, respectively, as shown elsewhere with polarized light microscopy [15]. Anthracene goes through an extended mesophase during carbonization to yield a graphitizable carbon. Sucrose carbonizes without the development of mesophase and a complete lack of anisotropy results. The isotropic sucrose char is a highly porous material as compared to anthracene coke and is non-graphitizable. The weight percentage (wt %) of oxygen in sucrose char found with EDS is 4.3. The sp^2 character as measured with EELS is $\sim 85\%$ (± 5) for both materials. The nanostructures are shown in the TEM micrographs in Figure 3A,B. The graphene segments have a preferential flow alignment in anthracene coke (Figure 3A). The directionality was induced during mesophase development. No such flow alignment is found in sucrose char. The nanostructure found in sucrose char has been said to be fullerene-like in nature and believed to be embedded with odd membered rings, predominantly pentagonal [24–28]. The d_{002} spacing as measured with XRD is 3.44 and 3.77 Å from anthracene coke and sucrose char respectively. The structural differences in these materials dictates the annealing trajectory upon increased HTT.

TEM micrographs after HTT of 1200 °C for a duration of 1 h are shown in Figure 3C,D. After heat treatment at 1200 °C, the nanostructure of anthracene coke shows improved packing and mutual orientation. The d_{002} spacing remains 3.44 Å. The chaotic nature of sucrose char nanostructure is more pronounced after heat treatment. Oxygen content is below the EDS detectable limit after heat treatment at 1200 °C. A synthetic graphite is produced from heat-treating anthracene coke at 2600 °C as displayed in the TEM micrograph in Figure 3E. Heat-treated sucrose char lacks long range order and is comprised of irregularly shaped cage-like structures ~ 5 –10 nm in width as displayed in the micrograph in Figure 3F. The cage-like structures are not projections of a curtain-like material as structure is not lost upon angle tilting in the TEM. Rouzaud and Oberlin have described this structure as a crumpled up sheet of paper [29]. The d_{002} lattice spacing as measured with XRD is 3.36 and 3.39 Å for anthracene coke and sucrose char after heat treatment at 2600 °C for 1 h. The lattice spacing results are in agreement with those reported for these two well studied materials [11,30,31].

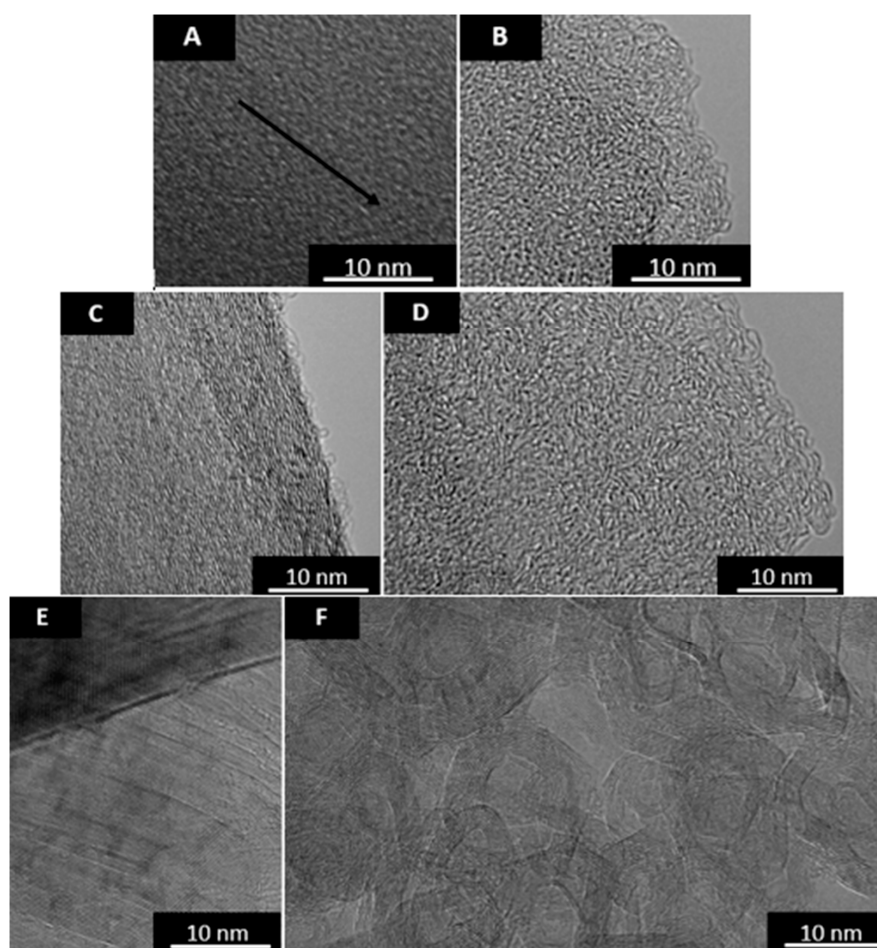


Figure 3. TEM micrographs of as prepared (A) anthracene coke (B) sucrose char. TEM micrographs of (C) anthracene coke (D) sucrose char-HTT 1200 °C for 1 h. TEM micrographs of (E) anthracene coke (F) sucrose char-HTT 2600 °C for 1 h.

3.2. CO₂ Laser Annealing

Laser pulse widths ranging from 0.25 to 300 s were used during CO₂ laser annealing experiments. The earliest detected temperature collected from the first few μ s of LII signal is approximately 1600 °C and temperature increases to a maximum of \sim 2600 °C over a duration of 1.4 ms. The maximum temperature is constant for the duration of the laser pulse. Use of the beam expander permits slower heating rates and lower maximum temperatures. No LII signal is detected during the first few ms of annealing with use of the beam expander. After a 5 ms delay, the samples reach \sim 1000 °C and a temperature of \sim 1200 °C is reached within an additional ms. A maximum temperature of \sim 1700 °C is reached over the duration of a second. Pulse width modulation was used in concert with the beam expander for the purpose of limiting maximum temperature to 1200 °C. Anthracene coke and sucrose char were laser heated to 1200 °C and 2600 °C and held for varying durations. The transformations are compared to traditional furnace heating at 1200 °C (Figure 3C,D) and 2600 °C (Figure 3E,F) for a 1 h duration.

3.2.1. CO₂ Laser Annealing—1200 °C

Samples were directly heated on copper supported lacey carbon TEM grids. The grids survive, for the most part, the short heating times at 1200 °C. Direct TEM grid heating is preferred as it provides the best way to evenly disperse the sample and assure uniform heating. Samples were crushed with a mortar and pestle, sonicated in methanol, and drop deposited on the TEM grids. The TTHs for sucrose

char and anthracene coke heated with a 20 s laser pulse are shown in Figure 4. Full power was used to heat the samples to the desired temperature of 1200 °C. Power was reduced to 85% for the remainder of the pulse duration. This power provides a stable isothermal temperature of 1200 °C throughout the laser pulse. Samples cool to temperatures below the detection limit of ~1000 °C in ~50 ms after laser pulse extinction.

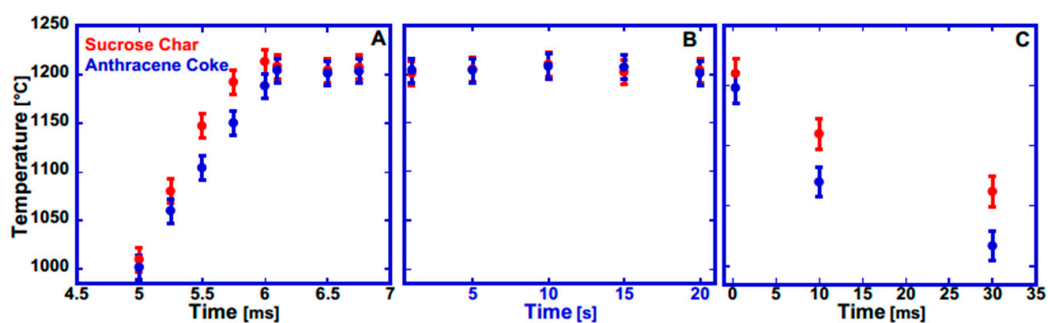


Figure 4. (A) Heating rates; (B) temperature stability during laser pulse (C) and cooling rates for anthracene coke and sucrose char heated with expanded beam CO₂ laser radiation.

At 1200 °C visible changes were subtle from samples heated for 1 s. The structures are shown in the TEM micrographs in Figure 5. Anthracene coke d_{002} spacing increases to 3.47 Å from 3.44 Å after laser annealing at 1200 °C for 1 s. This retrograde step is found in traditional HTT based experiments (long duration isothermal heating) where cokes reach a first L_c maximum and spacing minimum, followed by degradation with increasing HTT and then re-established order upon higher HTT [13,31]. However, the retrograde step has been reported to occur around 650 °C. Here it occurs at 1200 °C and thus this is a kinetic first step in annealing graphitizable carbons. The retrograde step can be explained by considering the initial nearly parallel alignment of the poly-aromatic hydrocarbons after mesophase development that then bond to neighbors that may not be in the same preferred orientation. Although the layer spacing is slightly increased, the material crystallinity increases as can be seen by the 002 arc spots in the SAED pattern insert in Figure 5A. This directionality is not as apparent in virgin anthracene coke (Figure A2). Both samples appear to have experienced a slight increase in lamellae length. The dark spots in the sucrose char micrograph are copper from melt expulsion of the Cu grid. TEM micrographs after annealing for 2.5 s are displayed Figure 6.

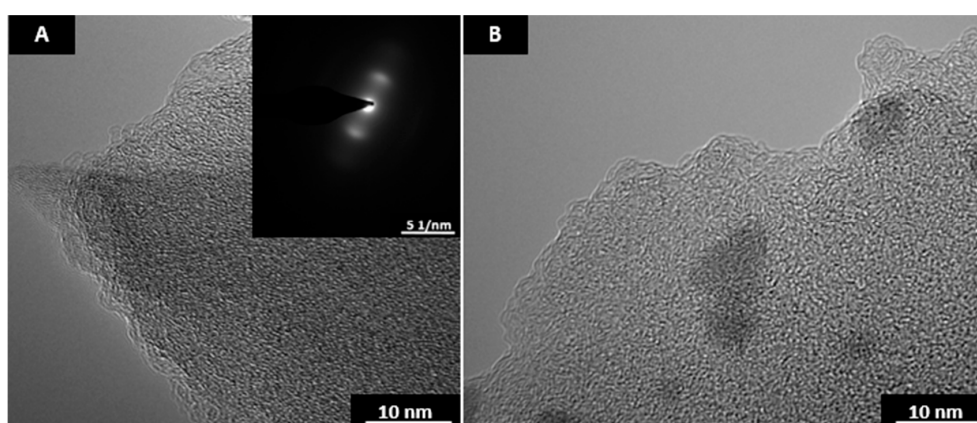


Figure 5. (A) TEM micrograph and SAED pattern of anthracene coke (B) and TEM micrograph of sucrose char after heat treatment at 1200 °C for 1s.

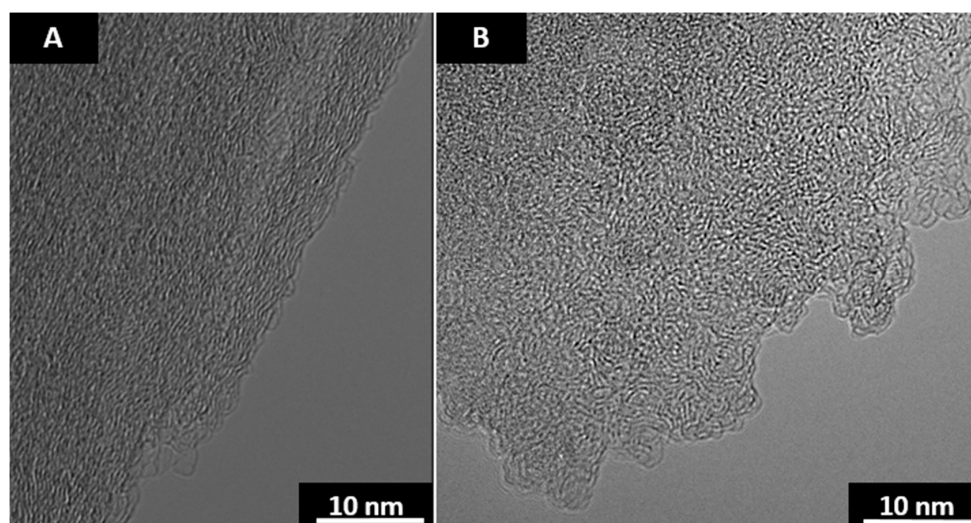


Figure 6. (A) TEM micrographs of anthracene coke (B) and sucrose char after heat treatment at 1200 °C for 2.5 s.

The laser annealed anthracene coke shown in Figure 6A is structurally equivalent to that found from furnace heating at 1200 °C for 1 h. As shown in Figure 6B, sucrose char structure after annealing at 1200 °C for 2.5 s is similar to furnace annealing for an hour, but yet incomplete as compared to the structure shown in Figure 3D. After 5 s at 1200 °C, sucrose char transformations are complete and the structure is equivalent to furnace annealing, as shown in the TEM micrograph in Figure 7.

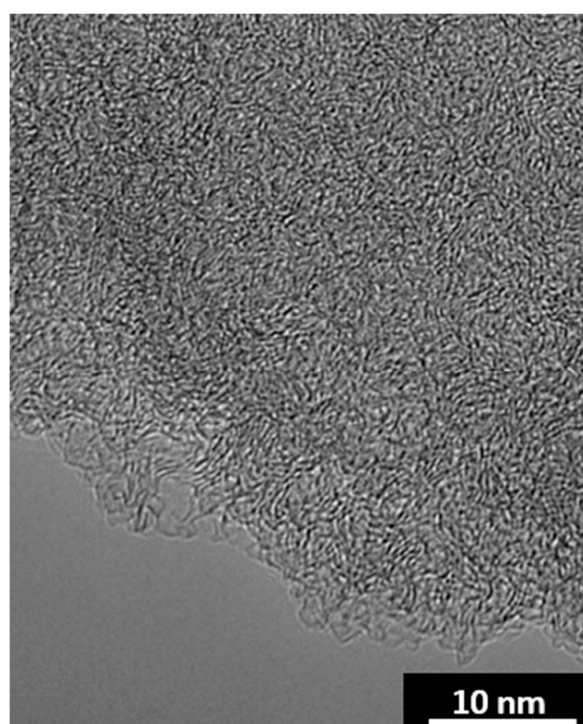


Figure 7. Sucrose char after heat treatment at 1200 °C for 5 s.

The transformation of sucrose char requires longer annealing time than anthracene coke to reach completion. Sucrose char lamellae have an arduous path towards restructuring due to the curvature and intertwined nature of the lamellae as compared to anthracene coke, which has rudimentary parallel

stacking due to mesophase development. Both samples anneal to furnace equivalent structures. Thus, CO₂ laser annealing is equivalent to furnace annealing at these conditions.

3.2.2. CO₂ Laser Annealing—2600 °C

To reach graphitization heat treatment temperature, the beam expander was removed and the laser was operated at full power. The TTHs for sucrose char and anthracene coke heated with a 20 s laser pulse are shown in Figure 8.

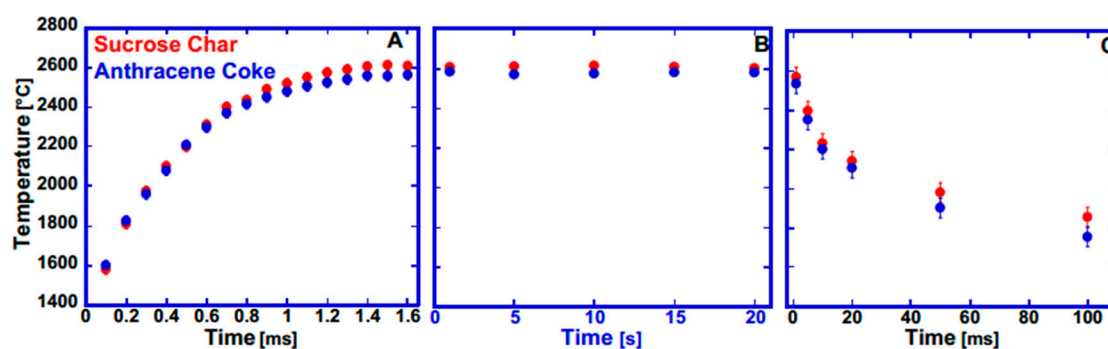


Figure 8. (A) Heating rates; (B) temperature stability during laser pulse (C) and cooling rates for anthracene coke and sucrose char heated with CO₂ laser radiation.

A maximum temperature of ~2600 °C is reached in 1.4 ms. The maximum temperature is isothermal throughout the laser pulse. Temperatures fall below 2000 °C within 100 ms, at which point material transformations are frozen in place.

At this temperature, the TEM grids do not survive. Samples were ground down to a fine powder and a very thin layer was directly heated in a small recessed hole in a graphite crucible. Thin samples were used to promote uniform heating. This approach was determined appropriate based on TTHs collected from underneath a thin layer. A carbon planchet with a hole drilled out for optical access was used to measure temperature from the underlying surface of the thin layer (couple hundred μm thickness). The thin layer was prepared by pressing a powdered sample into a self-supporting wafer. An aperture was used to collect LII signal from just the bottom of the laser-heated sample, avoiding contributions from the conductively heated planchet. A comparison of heating and maximum temperature from the top and bottom surfaces of sucrose char are displayed in Figure 9. Anthracene coke followed the same trend.

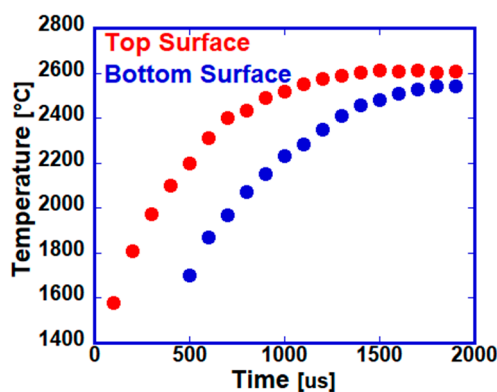


Figure 9. Heating rates and maximum temperature from the top and bottom surfaces of sucrose char.

Detectable LII signal is delayed 400 μs from the bottom relative to the top surface and an additional ~ 2 ms are required before the sample reaches thermal equilibrium. The bottom surface temperature remains ~ 50 $^{\circ}\text{C}$ less than the top surface.

CO_2 Laser Annealing of Anthracene Coke—2600 $^{\circ}\text{C}$

Annealing steps of graphitizable carbons follow the well-known thermodynamically based HTT steps as outlined by Oberlin [12]. Stage 1 at 500 $^{\circ}\text{C}$ represents the basic structural units (BSUs) formed from mesophase. Stage 2 occurs at 1000 $^{\circ}\text{C}$ when the BSUs associate face to face into distorted columns. Stage 3 occurs around 1500 $^{\circ}\text{C}$ when the columns coalesce into wrinkled layers. Stage 4 begins above 1700 $^{\circ}\text{C}$ when the distorted layers stiffen and become perfectly flat. Following the four stages, the layer plane spacing slowly decreases as layers assume graphitic lattice spacing at temperatures above 2200 $^{\circ}\text{C}$.

Noticeable restructuring occurs after annealing at 2600 $^{\circ}\text{C}$ for a duration of 0.25 s as displayed in the TEM micrograph in Figure 10. The crystalline directionality is more pronounced. An increase in crystalline order is clearly displayed in the SAED pattern. Virgin coke possess only diffuse diffraction rings as shown in Figure A2. After annealing for 0.25 s, arc spots are seen in the SAED pattern showing both the (002) and higher order (004) planes. This transition represents stage 2 (the BSUs associate face to face into distorted columns). The extent of transformation after 0.25 s at 2600 $^{\circ}\text{C}$ is equivalent to that of annealing at 1200 $^{\circ}\text{C}$ for a duration of 2.5 s and thus demonstrates the high rate dependence on temperature.

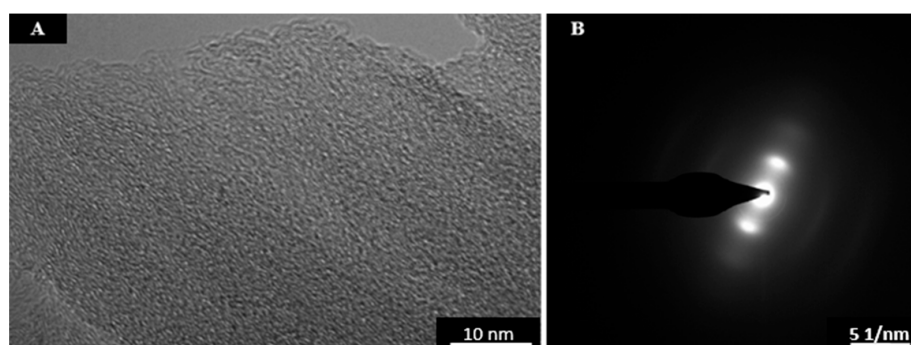


Figure 10. (A) TEM micrograph (B) and SAED pattern of anthracene coke after 0.25 s at 2600 $^{\circ}\text{C}$.

The distorted columns coalesce into wrinkled layers in stage 3 and occur within 1 s at 2600 $^{\circ}\text{C}$, as displayed in Figure 11A. After annealing for 5 s the layers become stiff and straight, Figure 11B, and represents the completion of the well-known annealing steps based on HTT. TEM micrographs after annealing for 1 and 5 min are provided in Figure A3.

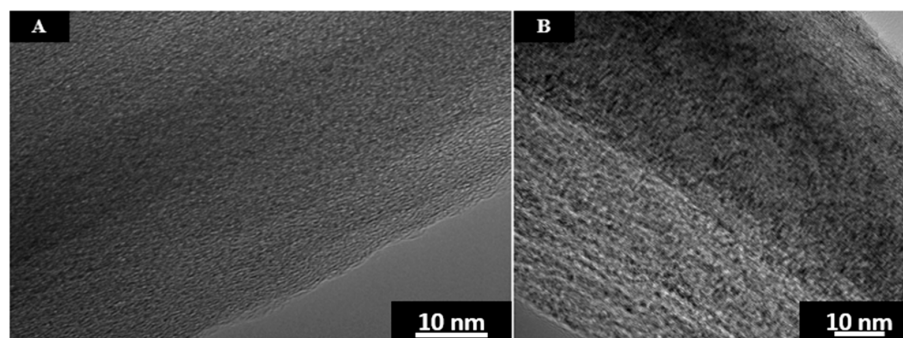


Figure 11. (A) TEM micrographs of anthracene coke after 1 s (B) and 5 s at 2600 $^{\circ}\text{C}$.

With additional annealing time, the ordering is best observed by the increase in crystallinity (3-dimensional graphitic order), measured by the decrease in d_{002} spacing, provided in Table 1. The 2-dimensional annealing steps and layer plane de-wrinkling are completed within the first 5 s above 2600 °C. Graphitization as quantified by a reduction in layer plane spacing below 3.44 Å does not occur until the completion of 2-dimensional ordering. Upon initiation of graphitization, the spacing reduction initially occurs at a faster rate and progressively slows. During the first 1 min of graphitization, the layer plane spacing decreases at a rate of 0.04 Å/min. After the first minute the rate of graphitization decays and a spacing reduction of only an additional 0.01 Å is achieved after an additional 4 min at 2600 °C (2.5×10^{-3} Å/min). The layer spacing from anthracene coke annealed in a furnace at 2600 °C for a duration of 1 h is 3.36. Thus, the spacing reduction between 5 min and 1 h may proceed at a rate of 5.5×10^{-4} Å/min. The trajectory and steps of annealing follow the traditional pathway. CO₂ laser annealing is equivalent to traditional annealing for this material at the conditions used.

Table 1. Layer plane spacing of anthracene coke with respect to time above 2600 °C.

Time (s)	d_{002} (Å)
0	3.44
0.25	3.44
1	3.44
5	3.42
60	3.40
300	3.39

CO₂ Laser Annealing of Sucrose Char—2600 °C

In this section, non-graphitizable sucrose char annealing trajectories with respect to time are observed. Sucrose char lamellae have an arduous path towards restructuring due to the curvature and intertwined nature of the lamellae in sucrose char as compared to anthracene coke. The pathway towards final annealed product is highlighted in the TEM micrographs shown in Figures 12–18. The end structure obtained after annealing for 30 s is equivalent to the structure found from traditional furnace heating at 2600 °C for a duration of 1 h. Therefore, CO₂ laser annealing is equivalent to traditional annealing for both graphitizable and non-graphitizable carbons at the conditions used in this study. Heating with a Q-switched Nd:YAG laser results in deviation from the traditional annealing pathway as illustrated in Appendix C. Considering that the final CO₂ laser annealed products are equivalent, the trajectories observed here during short annealing durations are also likely occurring in traditional furnace heating, yet undetectable due to limited temporal control.

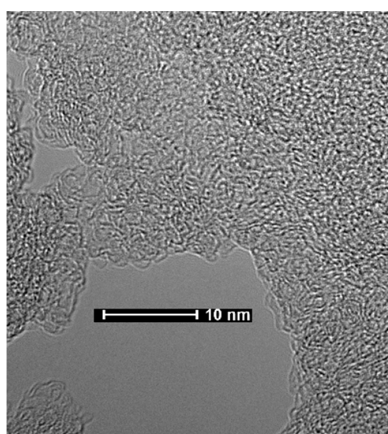


Figure 12. TEM micrograph of sucrose char after 0.25 s at 2600 °C.

The earliest observable material transformations occur after 0.25 s of annealing as displayed in Figure 12. Compared to the virgin char, the annealed sample lamellae appear slightly longer and have more pronounced curvature. The oxygen content is below the EDS detection limit. The structure after 0.25 s still has a long way to go before reaching the final thermal equilibrium structure. Oxygen is liberated early in the annealing process and acts to impact annealing trajectory via the structure it leaves behind upon evolution and not by direct cross-linking [15].

The structure after 1 s is shown in Figure 13. The arrow in the micrograph is highlighting what appears to be the early formation of a 2-layer quasi-spherical closed shell nanoparticle. The odd membered rings hypothesized to exist in sucrose char should lead to the formation of structures with high curvature as the neighboring lamellae bond together [24–28,32,33].

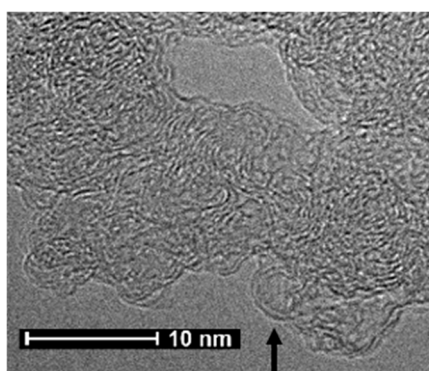


Figure 13. TEM micrograph of sucrose char after 1 s at 2600 °C.

The structure after annealing for 5 s is shown in Figures 14–16. The nanostructure is comprised entirely of quasi-spherical closed shell particles. This demonstrates that an abundance of odd membered rings are present. The spherical closed shell nanoparticles could not exist without inclusion of odd membered rings.

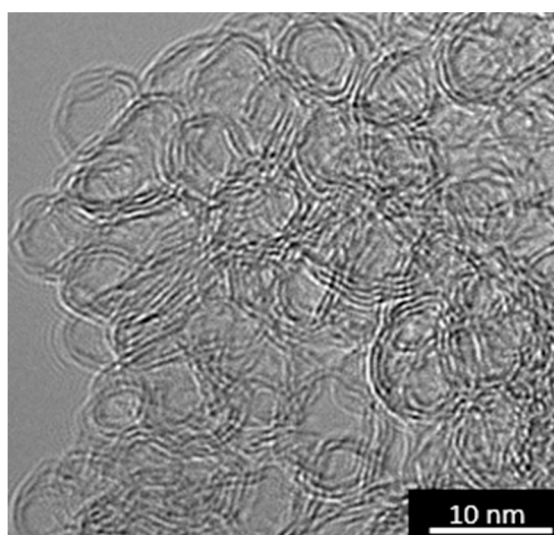


Figure 14. TEM micrograph of sucrose char after 5 s at 2600 °C.

A tilt series of TEM micrographs are provided in Figure 15 for the purpose of verifying the 3-dimensional shape (quasi-spherical). The presence of hollow shell structures is observed without stage rotation (B), and with stage rotation of 45° (C) the hollow shells are still observed and

can be compared against projections without stage rotation. The arrows in B and C highlight a hollow pentagonal shaped 3-layer particle. The hollow structure is not observed from projection at -45° (A), but rather the particles appear onion-like. The onion-like appearance at -45° is due to multiple projections.

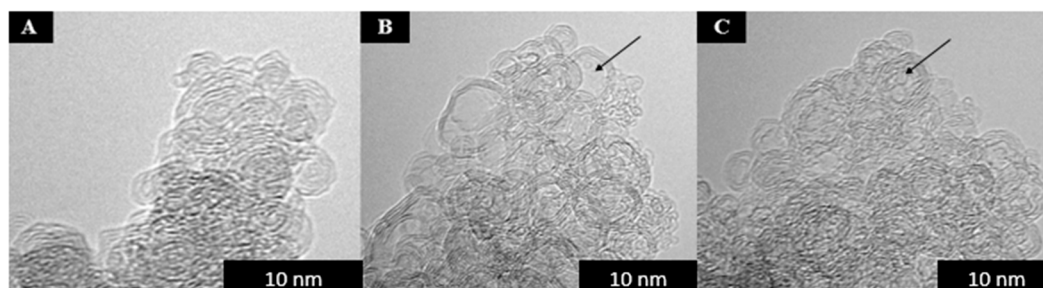


Figure 15. TEM micrographs of sucrose char after 5 s at 2600 °C. (A) Stage tilt: -45° ; (B) stage tilt 0° , (C) and stage tilt 45° .

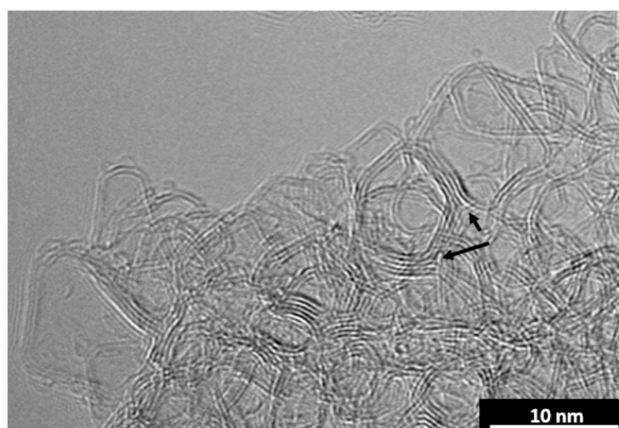


Figure 16. TEM micrograph of sucrose char after 5 s at 2600 °C.

For CO_2 laser annealing to be equivalent to furnace annealing, the closed shell structures must open upon additional heat treatment. The closed shell structures are obliterated with additional heat treatment and give rise to the formation of irregularly shaped pores formed from shell opening. Opened particles are displayed in the micrograph in Figure 17, taken after annealing for a duration of 10 s. SAED patterns highlighting shell opening are provided in Appendix D. Shell opening can be explained by considering the sharing of walls between particles and the extension of some of the wall layers extending out away from the particles. The bottom wall of the pentagonal shaped hollow particle (2-dimensional projection of a “house-like” structure) in Figure 16 is comprised of 5 layers. However, at the lower right corner, a couple layers branch off into the material and do not continuously wrap the particle (lower arrow in Figure 16). With additional annealing the layers that branch off will act to pull on the pentagonal particle and cause it to unravel. As the pentagonal structure opens it applies a stress on the already highly strained box-like particle it shares an upper wall with and causes it to open as well (upper arrow in Figure 16). This type of unraveling and propagative particle opening occurs throughout the material. The mechanism of initial closed shell formation followed by unraveling may explain the similar nanostructure found in some other non-graphitizable carbons. Glassy carbon produced from polyfurfuryl alcohol and carbons derived from anthrone and fluorene are a few such non-graphitizable carbons that have a similar nanostructure as compared to heat treated sucrose char [15].

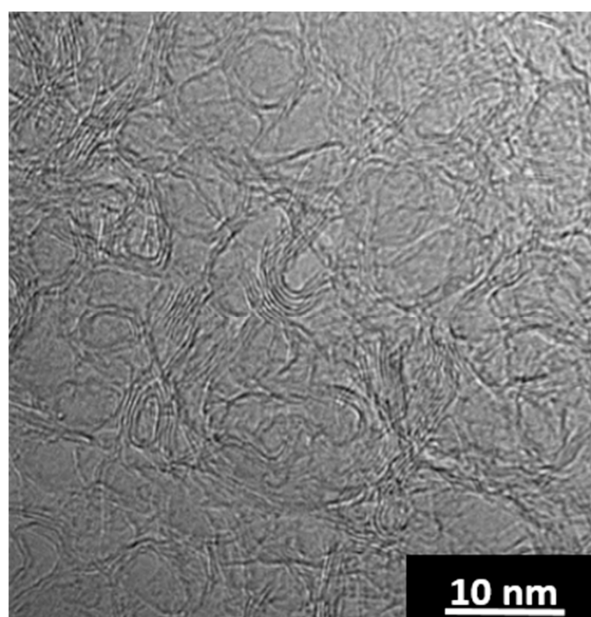


Figure 17. TEM micrographs of sucrose char after 10 s at 2600 °C.

The material continues to anneal with additional heat treatment and reaches an end structure that is equivalent to traditional furnace annealing in 30 s as displayed in Figure 18. The cage-like structures found in annealed sucrose char are the remnants of once closed quasi-spherical nanoparticles. Odd membered rings are required for the existence of such highly curved structures. Based on the temperature-time resolved series presented here, the odd membered rings in furnace annealed sucrose char are likely not manufactured during annealing via impinging growth, but rather present in the virgin char. Although highly disordered and comprised of curved cage-like structures, the degree of curvature in the end product is less than that after 5 s of annealing. The observed unfurling of the curvature requires that the odd membered rings, believed to be predominantly pentagonal, migrate to edges where their impact is minimized [34] and/or they are rearranged into hexagonal rings. Density functional theory has shown that migrating pentagonal rings on the zigzag edge of graphene may result in the overall loss of a pentagonal ring and formation of a hexagonal ring upon collision when mediated with hydrogen [35]. Such a mechanism may explain the unfurling of sucrose char.

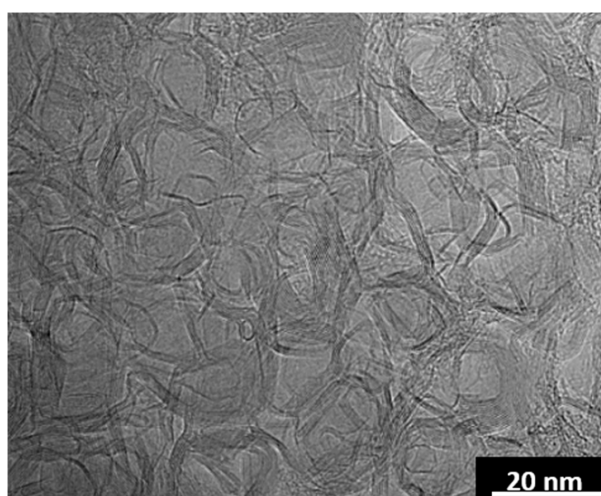


Figure 18. TEM micrograph of sucrose char after 30 s at 2600 °C.

3.3. ReaxFF Atomistic Simulation of Sucrose Char Unfurling

The observed unraveling of the closed shell structure was modeled and depicted in Figure 19. The simulations were carried out at 3327 °C for 0.1 ns. The initial structure does not vary significantly up to 0.01 ns. At ~0.04 ns, the carbon atoms from the inner shell start to break away and start migrating towards the outer shell. This leads to a reduction of curvature in the structure. As the structure evolves at 3327 °C, more inner shell atoms become part of the outer shell and increased unfurling of the structure is apparent after 0.1 ns. This indicates that a structure resembling a MWCNT is being formed from 2 multiwall spherical nanoparticles.

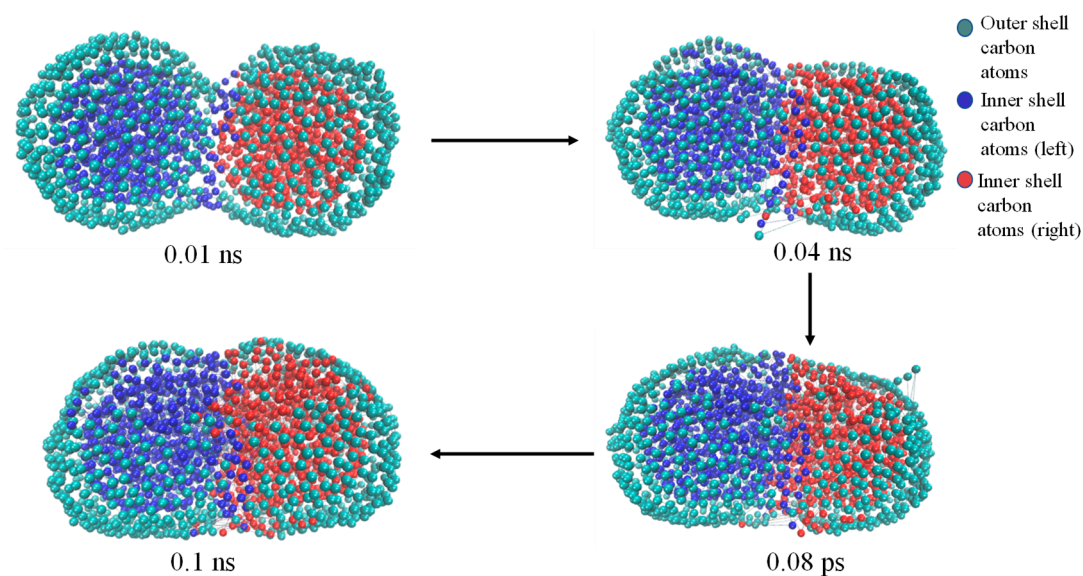


Figure 19. Atomistic model of carbon shell evolution at 3327 °C.

The initial structure at 3327 °C consists of 126 5-membered rings, 1240 6-membered rings and 51 7-membered rings. The number of carbon rings in the structure are tracked as the simulation evolves. This is depicted in Figure 20. There is no significant difference in the number of odd-numbered rings (5- and 7-membered rings) as the simulations progress. Collision loss of pentagonal ring systems was not observed on this limited time scale.

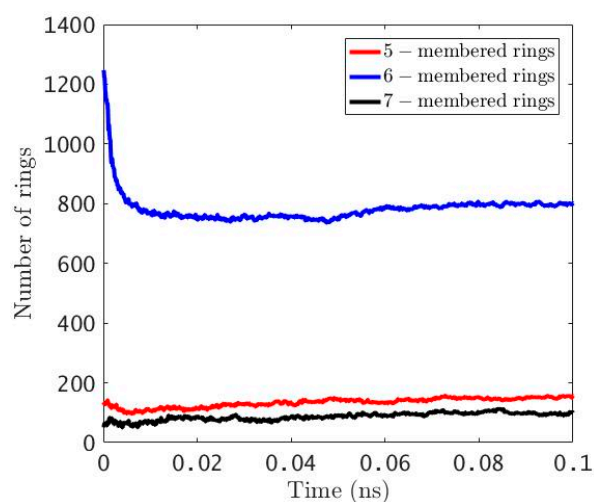


Figure 20. Evolution of carbon rings from atomistic simulation.

The result of the simulation is the formation of a structure resembling a MWCNT from two multiwall spherical nanoparticles. This lamellae unfurling and stacking is analogous to the annealing observed in peapod CNTs [36]. The encapsulated fullerenes in peapod CNTs coalesce into interior CNTs upon annealing [36]. The fullerenes are constrained in the peapod, whereas in sucrose char the spherical nanoparticles are not encapsulated and lead to cage-like structures and not CNTs.

4. Conclusions

A continuous wave CO₂ laser heats carbon samples to graphitization heat treatment temperature of 2600 °C in 1.4 ms. Samples followed traditional furnace annealing pathways based upon the equivalent end structures obtained from matching temperatures. Pulsing the CO₂ laser with a pulse generator enabled trajectories with respect to time above temperature to be followed. Graphitizable anthracene coke anneals faster than non-graphitizable sucrose char. Sucrose char passes through a structural state of completely closed shell nanoparticles that open upon additional heat treatment and give rise to the irregular pore structure found in the end product. The observed curvature in sucrose char annealed at 2600 °C is a result of shell opening and thus odd membered rings are not manufactured during the annealing process due to impinging growth of stacks, but are present in the starting structure.

Author Contributions: J.P.A. and R.L.V.W. conceived and designed the experiments; J.P.A. performed the experiments and material characterization; A.J. and A.C.T.v.D. conceived and designed the ReaxFF simulation; A.J. carried out the ReaxFF simulations; J.P.A. wrote the paper.

Funding: This work was supported by the NSF CBET, Grant No. 1236757 with the Pennsylvania State University, University Park, PA 16802.

Conflicts of Interest: The authors declare no conflict of interest.

Appendix A. Multi-Wavelength Pyrometry

The carbons used in this study are well approximated as black-body absorbers, as evident by good fit of Planck's black-body radiation curve to the laser induced incandescence (LII) signal as displayed in Figure A1. In particular, the LII spectra from the 2 materials at equivalent measured temperatures are the same. A dependence of emissivity on wavelength would manifest itself as discrepancies in the Planck black-body fit across the wavelength stretch, showing different temperatures for different regions of the spectra. Since this is not observed, the black-body approximation is justified.

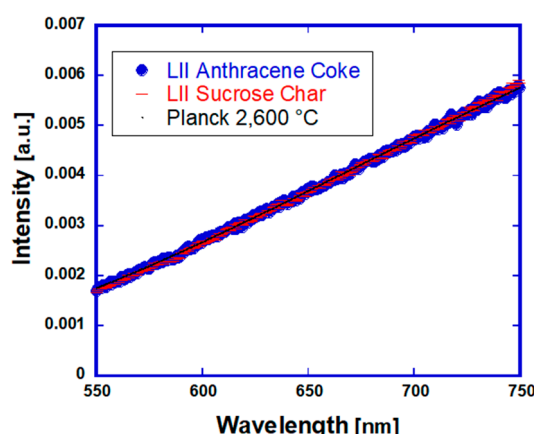


Figure A1. LII spectra from CO₂ laser heated anthracene coke and sucrose char fit to black-body distribution.

Appendix B. Anthracene Coke

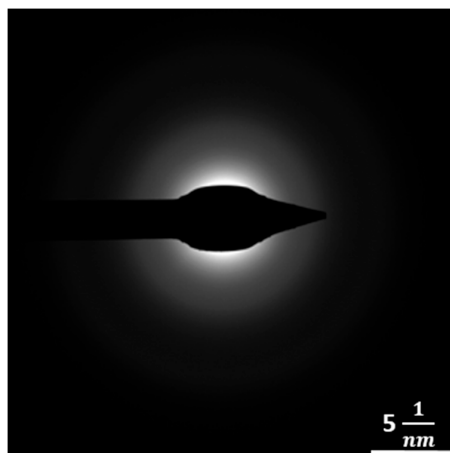


Figure A2. SAED pattern of virgin anthracene coke.

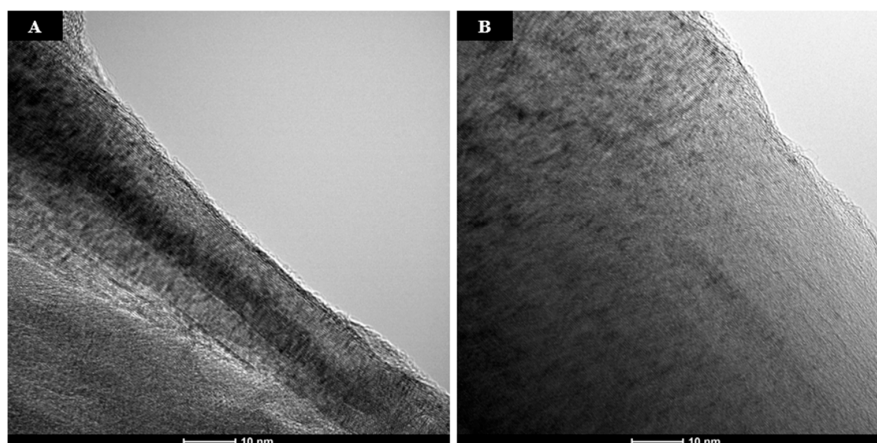


Figure A3. (A) TEM micrographs of anthracene coke after 1 min (B) and 5 min at 2600 °C.

Appendix C. Nd:YAG Laser Annealing

The Nd:YAG laser pulse width is fixed at ~ 8 ns as detailed in reference 8 [8]. The experimental control variable is the laser energy, measured in energy per unit area of the beam (laser fluence). Samples were heated under an argon atmosphere with fluences of 200, 100, and 50 mJ/cm^2 . These fluences are relatively low as compared to the available fluences in excess of 1500 mJ/cm^2 . At these fluences, samples are directly heated on lacey carbon TEM grids. Direct TEM grid heating is preferred as it provides the best way to evenly disperse the sample and assure uniform heating. Samples were crushed with a mortar and pestle, sonicated in methanol, and drop deposited on TEM grids. Low laser fluences were selected to avoid material sublimation, an undesired process when focus is on thermal annealing. The sublimation temperature of carbon materials is approximately 3700 °C [37,38]. The C_3 and C_2 sublimation temperatures have been reported to be 3864 °C and 4184 °C [39–41]. The peak temperatures reached with the fluences used here are ~ 2800 °C for 50 mJ/cm^2 , 3500 °C for 100 mJ/cm^2 , and 3950 °C for 200 mJ/cm^2 . Of the laser fluences used here only 200 mJ/cm^2 results in a maximum temperature above the sublimation point.

Detailed time temperature histories (TTHs) for sucrose char and anthracene coke heated with a 200 mJ/cm^2 laser pulse are shown in Figure A4. The error bars represent standard deviation from three repeated measurements. The time above 3700 °C is only 30 ns as can be seen from the first 100 ns TTH

curve. This is true for both sucrose char and anthracene coke as they have experimentally equivalent TTHs. The TTH is plotted out to 1700 °C, at which point incandescence signal is weak and the material transformations are frozen in place. The TTHs are divided into the first 100 ns and post 100 ns to illustrate the difference in cooling rate and to identify cooling mechanisms. Heating from ambient to ~3300 °C occurs within the first 2 ns of the laser pulse, temperature increases throughout the duration of the laser pulse and the maximum temperature reached is ~3900 °C. The maximum cooling rate of ~25 °C/ns from the first 5 ns following the laser pulse is attributed to sublimation. Once below the sublimation point, conductive cooling is the dominant heat loss mechanism. Radiative cooling is minor in comparison to conductive cooling at atmospheric pressure and higher. The cooling rate decreases as particles cool. The total time above 2200 °C is 1.5 μs.

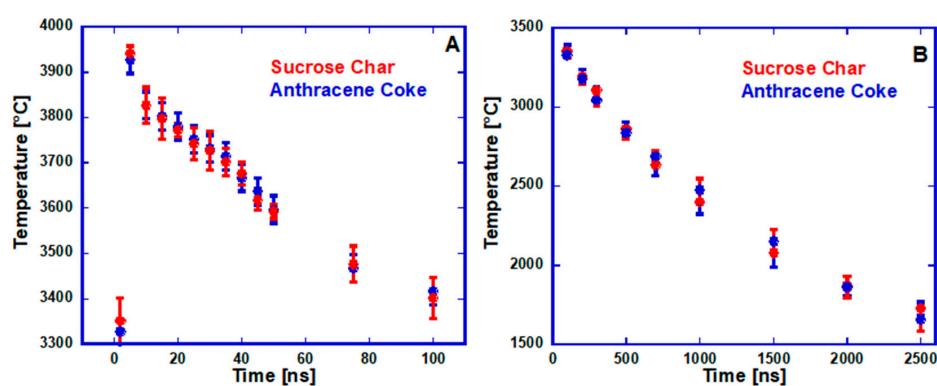


Figure A4. TTH of sucrose char and anthracene coke—200 mJ/cm²—(A) first 100 ns (B) post 100 ns.

The TEM images of laser heated anthracene coke are provided in Figure A5. Rather than annealing, the 200 mJ/cm² laser pulse ablated the anthracene coke. The energy dense pulse provides energy in excess of all the annealing activation energies. Thus, all activation energies including: devolatilization, conversion of sp³ hybridized carbon to sp² hybridized carbon, lamellae mobilization and growth, reorientation, de-wrinkling, and alignment (*d*-spacing), occur almost simultaneously. Furnace annealing has a much slower energy addition rate and therefore traditional furnace annealing steps are delayed based on heating rate and occur in a step wise fashion. By providing the energy needed for lamellae to become highly mobile prior to growth and reorientation acting to anchor them down, they are able to break free of the material. Upon rapid cooling, the ablated layers form the chaotic fullerene-like nanostructure out of necessity to terminate reactive edge sites, structure shown in Figure A5B.

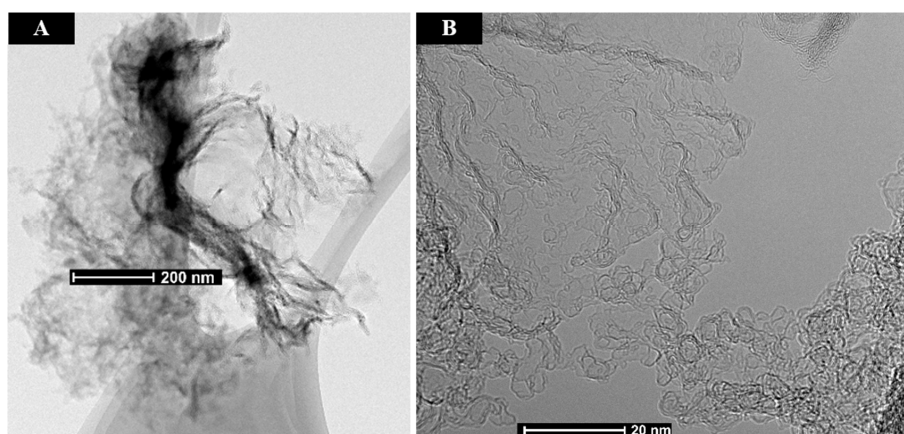


Figure A5. (A,B) TEM images of anthracene coke—200 mJ/cm².

TEM images of sucrose char after laser heating with a $200 \text{ mJ}/\text{cm}^2$ laser pulse are provided in Figure A6. Most of the starting 4.1 wt % oxygen in sucrose char is liberated. The oxygen content in the EDS elemental map in Figure A6A is 0.9 wt %. The retained oxygen may be due to kinetic constraints imposed by rapid cooling, some of the liberated oxygen may be reincorporated into the carbon matrix upon cooling, or surface oxygen [15]. The EDS map also highlights the carbon thickness contrast and the heterogeneity in the structure is characteristic of ablation. The nanostructure of sucrose char is similar to that found after annealing at $1200 \text{ }^\circ\text{C}$ for a duration of 1 h. The major structure type found is lamellae with only a couple layers per stack that are curved at multiple points and are highly intertwined with neighboring material. A few regions possess more order with longer L_a and thicker L_c , like that shown in Figure A6C. For sucrose char, similarities appear between Nd:YAG laser and traditional annealing. The TTHs for sucrose char and anthracene coke heated with a $100 \text{ mJ}/\text{cm}^2$ laser pulse are shown in Figure A7.

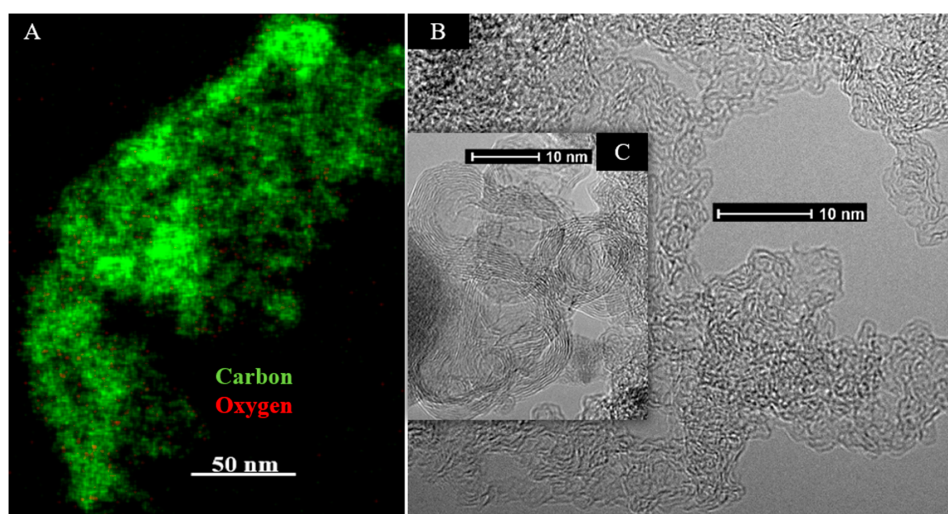


Figure A6. (A) EDS map (B,C) TEM micrographs of sucrose char— $200 \text{ mJ}/\text{cm}^2$.

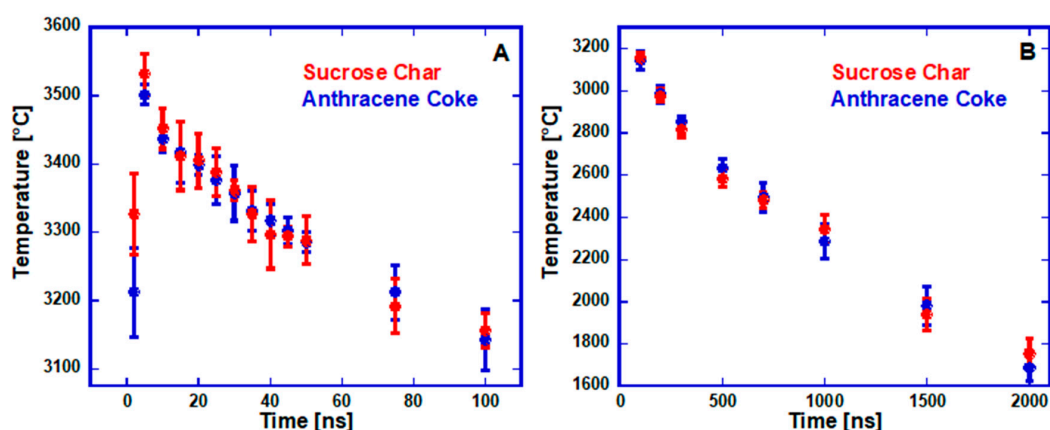


Figure A7. TTHs of sucrose char and anthracene coke— $100 \text{ mJ}/\text{cm}^2$ —(A) first 100 ns (B) post 100 ns.

Although the maximum temperature is well below the sublimation point, the first 5 ns of cooling after peak temperature occur at a rate ($15 \text{ }^\circ\text{C}/\text{ns}$), faster than the possible combination of conductive and radiative cooling mechanisms alone. This rapid initial cooling, not caused via vaporization, must be due to material ablation. Following the initial cooling, the TTH profiles follow the same trend as previously discussed. Anthracene coke and sucrose char have similar material properties upon Nd:YAG laser heating, shown in the TEM micrographs in Figure A8.

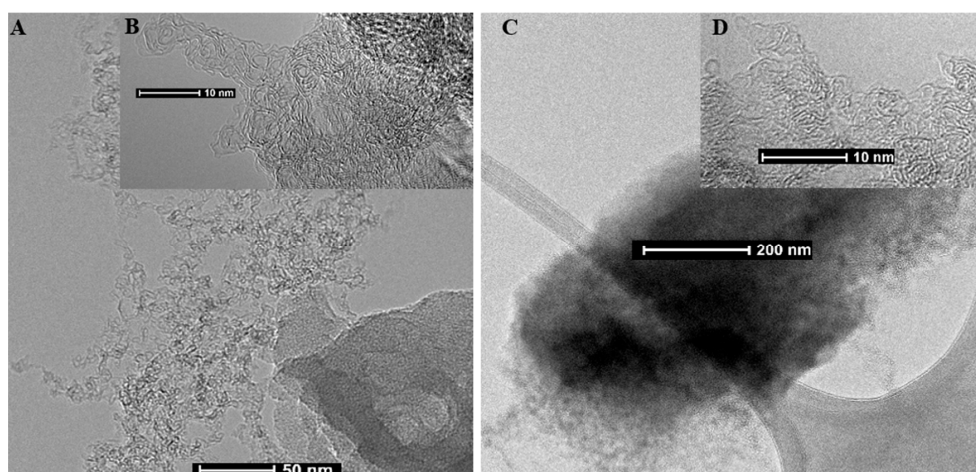


Figure A8. TEM micrographs after laser heating with $100 \text{ mJ}/\text{cm}^2$ —(A,B) anthracene coke (C,D) and sucrose char.

The overall extent of ablation is less between the 100 and $200 \text{ mJ}/\text{cm}^2$ laser heated samples. The interiors of the particles from both anthracene and sucrose are unaltered after laser heating with $100 \text{ mJ}/\text{cm}^2$ laser pulse. This is due to the limited skin depth of 1064 nm laser light. With decreasing laser energy the depth of heating decreases.

The TTHs for sucrose char and anthracene coke heated with a $50 \text{ mJ}/\text{cm}^2$ laser pulse are shown in Figure A9.

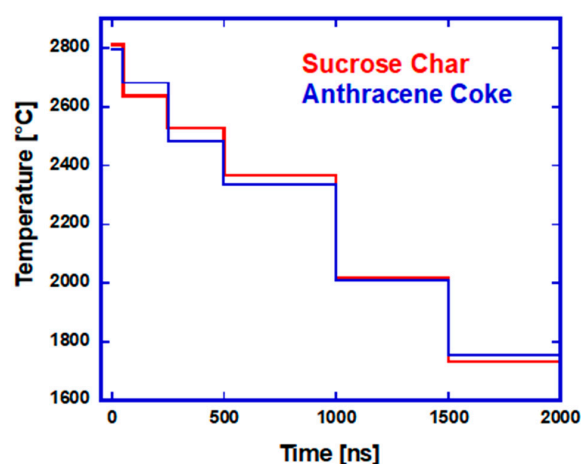


Figure A9. TTHs of sucrose char and anthracene coke— $50 \text{ mJ}/\text{cm}^2$.

The low fluence results in low incandescence signal and wider camera gate widths are required to collect adequate signal for temperature determination. The TTHs in Figure A9 are integrated average temperatures, with collection widths as wide as 500 ns . The peak temperature of $\sim 2800 \text{ }^\circ\text{C}$ is the integrated average temperature of the first 50 ns of incandescence signal. The true peak temperature occurring just after the laser pulse is likely higher. For example, the peak temperature found with a 5 ns gate width from $200 \text{ mJ}/\text{cm}^2$ is $3940 \text{ }^\circ\text{C}$ and the average integrated temperature from the first 50 ns is $3850 \text{ }^\circ\text{C}$. The average of 10 measurements taken in 5 ns intervals over the first 50 ns from $200 \text{ mJ}/\text{cm}^2$ is $3760 \text{ }^\circ\text{C}$. The first 50 ns time integrated temperature is higher than the average of the 10 temperature measurements taken in 5 ns intervals over the first 50 ns of LII signal. This is because higher temperatures have higher radiative intensity and thus integrated average temperatures are

biased to the higher initial temperatures. Due to the low incandescence signal at 50 mJ/cm^2 , the initial cooling rate immediately after peak temperature is unknown and cannot be used to make inference about the possibility of ablation based on the TTH alone. The total incandescence signal is related to both maximum temperature and quantity of heated sample. Limited transformed sample was found upon TEM investigation, small regions of annealed/ablated material were found and shown in the TEM micrographs in Figure A10. The anthracene coke structure in Figure A10A is more graphitic as compared to heating with high laser fluences, graphitic bands are seen in the ablated material. The laser heated material is not fully ablated (discharged) from the material as it is still connected to the original particles. It appears that the heated surface layers are peeled off and expand out away from the relatively cool underlying particle. Anthracene coke was used for multiple pulse heating as a variation in annealing trajectory relative to traditional heating is more easily seen from this sample. Micrographs after heating with 10 pulses of 50 mJ/cm^2 are provided in Figure A11.

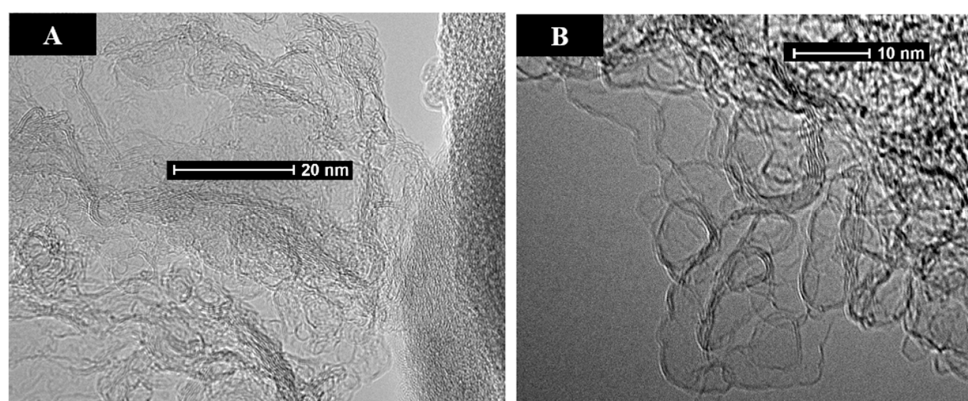


Figure A10. (A) TEM micrographs of anthracene coke (B) and sucrose char— 50 mJ/cm^2 .

The structure after 10 pulses is fullerene-like and comprised mainly of $\sim 5\text{--}10 \text{ nm}$ closed shell quasi-spherical particles. This shows that even at low laser fluences, the energy dense Q-switched laser pulses cannot be used to study annealing at these short timescales. Material ablation is unavoidable at these rapid heating rates $\sim 3.3 \times 10^{11} \text{ }^\circ\text{C/s}$ and short time at elevated temperature. Rapid heating causes the initial deviation from traditional furnace annealing pathway by simultaneously activating all activation energies. Kinetics also play a role in annealing pathway as the time at elevated temperature is limited (time above $2000 \text{ }^\circ\text{C}$ is $1.5 \text{ } \mu\text{s}$). At this limited time above the threshold temperature, the long-range material motions are kinetically limited. Regardless of additional pulses, the total consecutive time at temperature is never long enough for long-range material restructuring to occur.

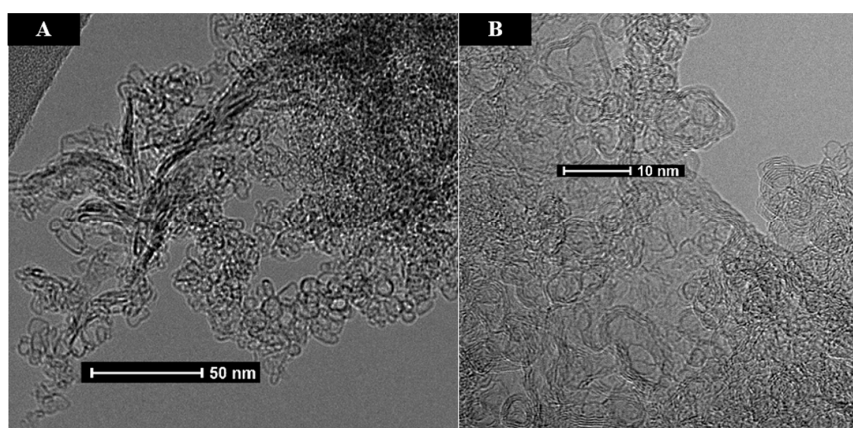


Figure A11. (A,B) TEM micrographs of anthracene coke—10 pulse— 50 mJ/cm^2 .

Appendix D. CO₂ Laser Annealed Sucrose Char SAED Patterns

Virgin sucrose char possess only diffuse diffraction rings from the (002), (100), and (004) planes as displayed in Figure A12A. The material is highly amorphous with minimal lamellae stacking as inferred from the diffuse 3-dimensional (002) and (004) rings. No crystal directionality is present in this material. After annealing for 1 s at 2600 °C, narrowing of the diffraction rings is observed as a result of material restructuring. However, directionality is yet absent as displayed by the diffuse ring patterns in Figure A12B. The quasi-spherical nanoparticles found after 5 s are zero dimensional and thus an absence of directionality in the SAED pattern is expected. After annealing for 5 s at 2600 °C the rings remain diffuse and absent of directionality as displayed in Figure A12C. Upon shell opening and unfurling of the curved nanostructure, elongated stacks of carbon lamellae are found after annealing for 10 s. These nanoscale regions of local crystal order and directionally give rise to the (002) arc spots in Figure A12D.

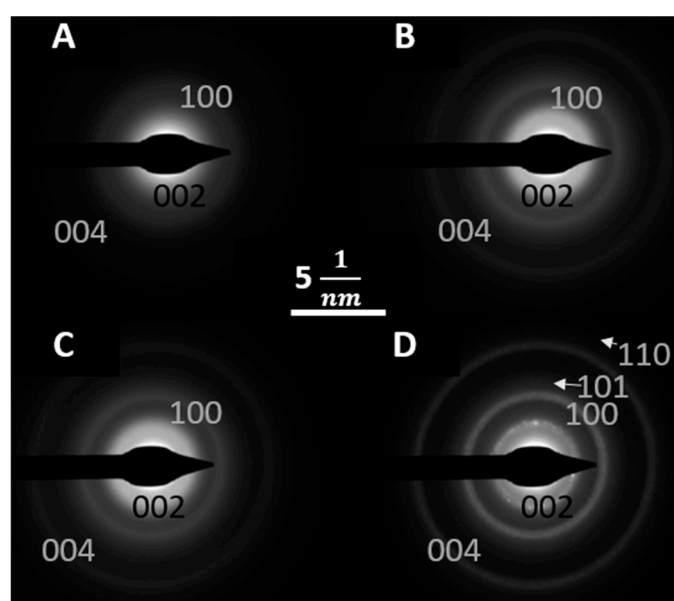


Figure A12. SAED patterns from sucrose char (A) virgin (B) after annealing at 2600 °C for 1 s (C) after annealing at 2600 °C for 5 s and (D) after annealing at 2600 °C for 10 s.

References

1. Fair, F.V.; Collins, F.M. Effect of residence time on graphitization at several temperatures. In *Proceedings of the Fifth Conference on Carbon*; Pergamon Press: New York, NY, USA, 1961; pp. 503–508.
2. Mizushima, S. Rate of graphitization of carbon. In *Proceedings of the Fifth Conference on Carbon*; Pergamon Press: New York, NY, USA, 1961; p. 439, ISBN 9780080097084.
3. Fischbach, D.B. The kinetics and mechanism of graphitization. In *Chemistry and Physics of Carbon*; Walker, P.L., Ed.; Marcel Dekker, Inc.: New York, NY, USA, 1971; pp. 1–92.
4. Emmerich, F.G. Evolution with heat treatment of crystallinity in carbons. *Carbon* **1995**, *33*, 1709–1715. [[CrossRef](#)]
5. Murty, H.N.; Biederman, D.L.; Heintz, E.A. Kinetics of graphitization-I. Activation energies. *Carbon* **1969**, *7*, 667–681. [[CrossRef](#)]
6. Fischbach, D.B. Kinetics of graphitization of a petroleum coke. *Nature* **1963**, *200*, 1281–1283. [[CrossRef](#)]
7. Putman, K.J.; Sofianos, M.V.; Rowles, M.R.; Harris, P.J.F.; Buckley, C.E.; Marks, N.A.; Suarez-Martinez, I. Pulsed thermal treatment of carbon up to 3000 °C using an atomic absorption spectrometer. *Carbon* **2018**, *135*, 157–163. [[CrossRef](#)]
8. Abrahamson, J.P.; Madhu, S.; Mathews, J.P.; Vander Wal, R.L. Pulsed laser annealing of carbon black. *Carbon* **2017**, *124*, 380–390. [[CrossRef](#)]

9. Abrahamson, J.P.; Rajagopalan, R.; Vander Wal, R.L. Porous (swiss-cheese) graphite. *C* **2018**, *4*, 27. [[CrossRef](#)]
10. Franklin, R.E. The interpretation of diffuse X-ray diagrams of carbon. *Acta Crystallogr.* **1950**, *3*, 107–121. [[CrossRef](#)]
11. Franklin, R.E. Crystallite growth in graphitizing and non-graphitizing carbons. *Proc. R. Soc. Lond. A Math. Phys. Eng. Sci.* **1951**, *209*, 196–218. [[CrossRef](#)]
12. Oberlin, A. Carbonization and graphitization. *Carbon* **1984**, *22*, 521–541. [[CrossRef](#)]
13. Marsh, H.; Crawford, D. Structure in graphitizable carbon from coal-tar pitch HTT 750–1148 K. Studied using high resolution electron microscopy. *Carbon* **1984**, *22*, 413–422. [[CrossRef](#)]
14. Kinney, C.R.; Nunn, R.C.; Walker, P.L. Carbonization of anthracene and graphitization of anthracene carbons. *Ind. Eng. Chem.* **1957**, *49*, 880–884. [[CrossRef](#)]
15. Abrahamson, J.P.; Jain, A.; van Duin, A.C.T.; Vander Wal, R.L. Carbon structure and resulting graphitizability upon oxygen evolution. *Carbon* **2018**, *135*, 171–179. [[CrossRef](#)]
16. Van Duin, A.C.T.; Dasgupta, S.; Lorant, F.; Goddard, W.A. ReaxFF: A reactive force field for hydrocarbons. *J. Phys. Chem. A* **2001**, *105*, 9396–9409. [[CrossRef](#)]
17. Brenner, D.W. Empirical potential for hydrocarbons for use in simulating the chemical vapor deposition of diamond films. *Phys. Rev. B* **1990**, *42*, 9458–9471. [[CrossRef](#)]
18. Chenoweth, K.; van Duin, A.C.T.; Goddard, W.A. ReaxFF reactive force field for molecular dynamics simulations of hydrocarbon oxidation. *J. Phys. Chem. A* **2008**, *112*, 1040–1053. [[CrossRef](#)] [[PubMed](#)]
19. Wang, Q.D.; Wang, J.B.; Li, J.Q.; Tan, N.X.; Li, X.Y. Reactive molecular dynamics simulation and chemical kinetic modeling of pyrolysis and combustion of *n*-dodecane. *Combust. Flame* **2011**, *158*, 217–226. [[CrossRef](#)]
20. Castro-Marcano, F.; Kamat, A.M.; Russo, M.F.; van Duin, A.C.T.; Mathews, J.P. Combustion of an Illinois No. 6 coal char simulated using an atomistic char representation and the ReaxFF reactive force field. *Combust. Flame* **2012**, *159*, 1272–1285. [[CrossRef](#)]
21. Liu, L.; Bai, C.; Sun, H.; Goddard, W.A. Mechanism and kinetics for the initial steps of pyrolysis and combustion of 1,6-dicyclopropane-2,4-hexyne from ReaxFF reactive dynamics. *J. Phys. Chem. A* **2011**, *115*, 4941–4950. [[CrossRef](#)] [[PubMed](#)]
22. Berendsen, H.J.C.; Postma, J.P.M.; Van Gunsteren, W.F.; Dinola, A.; Haak, J.R. Molecular dynamics with coupling to an external bath. *J. Chem. Phys.* **1984**, *81*, 3684–3690. [[CrossRef](#)]
23. Ashraf, C.; van Duin, A.C.T. Extension of the ReaxFF combustion force field toward syngas combustion and initial oxidation kinetics. *J. Phys. Chem. A* **2017**, *121*, 1051–1068. [[CrossRef](#)] [[PubMed](#)]
24. Harris, P.J.F. New perspectives on the structure of graphitic carbons. *Crit. Rev. Solid State Mater. Sci.* **2005**, *30*, 235–253. [[CrossRef](#)]
25. Harris, P.J.F.; Tsang, S.C. High-resolution electron microscopy studies of non-graphitizing carbons. *Philos. Mag. A Phys. Condens. Matter Struct. Defects Mech. Prop.* **1997**, *76*, 667–677. [[CrossRef](#)]
26. Harris, P.J.F. Impact of fullerenes on carbon science. In *Chemistry and Physics of Carbon*; Radovic, L.R., Ed.; Marcel Dekker, Inc.: New York, NY, USA, 2003; pp. 1–36.
27. Harris, P.J.F. Fullerene-related structure of commercial glassy carbons. *Philos. Mag.* **2004**, *84*, 3159–3167. [[CrossRef](#)]
28. Harris, P.J.F. Structure of non-graphitising carbons. *Int. Mater. Rev.* **1997**, *42*, 206–218. [[CrossRef](#)]
29. Rouzaud, J.N.; Oberlin, A. Structure, microtexture, and optical properties of anthracene and saccharose-based carbons. *Carbon* **1989**, *27*, 517–529. [[CrossRef](#)]
30. Franklin, R.E. The structure of graphitic carbons. *Acta Crystallogr.* **1951**, *4*, 253–261. [[CrossRef](#)]
31. Lewis, I. Chemistry of carbonization. *Carbon* **1982**, *20*, 519–529. [[CrossRef](#)]
32. Harris, P.J.F.; Green, M.L.H.; Tsang, S.C. High-resolution electron microscopy of tubule-containing graphitic carbon. *J. Chem. Soc. Faraday Trans.* **1993**, *89*, 1189. [[CrossRef](#)]
33. Harris, P. Transmission electron microscopy of carbon: A brief history. *C* **2018**, *4*, 4. [[CrossRef](#)]
34. Whitesides, R.; Domin, D.; Salomon-Ferrer, R.; Lester, W.A.; Frenklach, M. Graphene layer growth chemistry: Five- and six-member ring flip reaction. *J. Phys. Chem. A* **2008**, *112*, 2125–2130. [[CrossRef](#)] [[PubMed](#)]
35. Whitesides, R.; Kollias, A.C.; Domin, D.; Lester, W.A.; Frenklach, M. Graphene layer growth: Collision of migrating five-member rings. *Proc. Combust. Inst.* **2007**, *30*, 539–546. [[CrossRef](#)]
36. Smith, B.W.; Luzzi, D.E. Formation mechanism of fullerene peapods and coaxial tubes: A path to large scale synthesis. *Chem. Phys. Lett.* **2000**, *321*, 169–174. [[CrossRef](#)]

37. Abrahamson, J. Graphite sublimation temperatures, carbon arcs and crystallite erosion. *Carbon* **1974**, *12*, 111–141. [[CrossRef](#)]
38. Michelsen, H.A.; Schulz, C.; Smallwood, G.J.; Will, S. Laser-induced incandescence: Particulate diagnostics for combustion, atmospheric, and industrial applications. *Prog. Energy Combust. Sci.* **2015**, *51*, 2–48. [[CrossRef](#)]
39. Michelsen, H.A.; Schrader, P.E.; Goulay, F. Wavelength and temperature dependences of the absorption and scattering cross sections of soot. *Carbon* **2010**, *48*, 2175–2191. [[CrossRef](#)]
40. Goulay, F.; Schrader, P.E.; Lopez-Yglesias, X.; Michelsen, H.A. A data set for validation of models of laser-induced incandescence from soot: Temporal profiles of LII signal and particle temperature. *Appl. Phys. B Lasers Opt.* **2013**, *112*, 287–306. [[CrossRef](#)]
41. Michelsen, H.A.; Liu, F.; Kock, B.F.; Bladh, H.; Bioarciuc, A.; Charwath, M.; Dreier, T.; Hedef, R.; Hofmann, M.; Reimann, J.; et al. Modeling laser-induced incandescence of soot: A summary and comparison of LII models. *Appl. Phys. B* **2007**, *87*, 503–521. [[CrossRef](#)]



© 2018 by the authors. Licensee MDPI, Basel, Switzerland. This article is an open access article distributed under the terms and conditions of the Creative Commons Attribution (CC BY) license (<http://creativecommons.org/licenses/by/4.0/>).